Structural Mechanisms of the Cooling Rate Effect on the Deformation Behaviors in Metallic Glasses

Bian Zhou[1] · Ming-fei Li[1] · Fan Xiong[1] · Liang Yang[1]

Abstract

In this work, the structural mechanisms of the cooling rate effect on the deformation behaviors in metallic glasses (MGs) is studied, by performing the synchrotron radiation-based experiments coupled with a series of simulations. It is found that a MG prepared at lower cooling rate has the higher yield strength and is more likely to soften itself, resulting in lower plasticity. This is because some atomic-to-cluster level structural factors, such as coordination numbers, atomic packing efficiencies, cluster concentrations and regularities. In addition, a quantitative analysis reveals that higher cooling rate leads to more free volumes, and significantly affect the evolution of free volumes during the compressive deformation, tuning the formation and the evolution of shear transformation zones, as well as the yield strength and the plasticity.

Keywords Metallic glasses · Synchrotron radiation · Molecular dynamics · Cooling rate · Compressive deformation · Microstructure

1 Introduction

Metallic glasses (MGs) have attracted great attention for decades [1], owing to the unique physical [2, 3], chemical [4], and mechanical properties [5, 6]. As we know, MGs are usually prepared by quenching metallic melt at a relatively high cooling rate [7–9] to retard the atomic diffusion, so that the liquid structure can be preserved in the amorphous solid [10]. If the cooling rate is largely reduced, atoms have enough time to rearrange themselves, leading to the formation of crystal structure instead. It was suggested that MGs prepared at different cooling rates also may affect their atomic arrangements and lead to fine structural difference, although all of them are full amorphous [11]. In addition, it has been revealed that the cooling rate in vitrifying one alloy from the liquid affects its properties [12–16]. Meanwhile, it is apparent that the casting size of MGs varies with the cooling rate [17–19]. It was suggested that size effect controls the mechanical properties in MGs. For instance, it was revealed that the as-cast bulk MGs had higher elastic

moduli and hardness [19] and worse plasticity [12] than the ribbon samples with the same composition, while thin wire MG samples showed lower elastic moduli [20].

Since the mechanical behaviors of MGs are influenced by both the cooling rate and the size effect, and the casting size of a MG is closely linked up with its cooling rate [21], making it difficult to distinguish the dependence of the deformation behaviors on the cooling rate or the casing size. Therefore, a question is raised: Can we reveal the essential mechanism of deformation behaviors in MGs prepared at different cooling rates, excluding the influence of size effect?

In this work, a $Zr_{48}Cu_{45}Al_7$ ternary composition was selected as a research prototype. The microstructures and the deformation behaviors of two $Zr_{48}Cu_{45}Al_7$ MGs prepared at different cooling rates were studied, by using the state-of-the-art synchrotron radiation-based experiments coupled with a series of simulations.

2 Experiment and Simulation Methods

2.1 Sample Preparation

The alloy ingots were prepared by arc-melting the mixture of Zr, Cu, and Al elements with purities of 99.9 wt% in Ti-gettered high-purity argon atmosphere (99.9999%). The

---

✉ Liang Yang
 yangliang@nuaa.edu.cn

1   College of Materials Science and Technology, Nanjing
    University of Aeronautics and Astronautics, Nanjing 210016,
    People's Republic of China

ingots were melted at least 5 times in order to achieve their compositional homogeneity. The $Zr_{48}Cu_{45}Al_7$ ribbons with a cross section of 0.04×2 mm and the $Zr_{48}Cu_{45}Al_7$ rods with a diameter of 6 mm were prepared by melt spinning and copper-mold suction casting, respectively [22]. The cooling rates (R) for ribbon and rod samples are about 2×10^6 K s^{-1} and 1×10^2 K s^{-1} respectively, which were estimated from the size of the minimum dimensions of these samples, by using,

$$R = \frac{A}{t^2} \tag{1}$$

where t is thickness of the casting samples and A is 3840 mm^2 K s^{-1} [23]. Although the R values are not very accurate, it is sufficient to indicate the large difference of cooling rate in these two samples.

2.2 Synchrotron Radiation-Based Experiments

To achieve the proper penetrating depth in the diffraction measurement, the rod sample was cut into a slice having a dimension of 1 mm. The ribbon samples were piled up with a thickness also about 1 mm in a capillary. Room temperature X-ray diffraction (XRD) measurements were performed for both samples, using a high-energy synchrotron radiation monochromatic beam (about 103.8 keV) on beam line BW5 in Hasylab. Two-dimension diffraction data was collected by using a Mar345 image plate, and integrated to Q-space (Q is the wave vector transfer) after subtracting the corresponding background by using the program Fit2D [24]. The output data was normalized by software PDFgetX to obtain the structure factor [S(Q)] according to the Faber–Ziman equation [25].

Subsequently, Zr and Cu K-edge extended X-ray absorption fine structure (EXAFS) measurements were carried out for both samples using a transmission mode at beam line BL14W1, in the Shanghai Synchrotron Radiation Facility (SSRF) of China. Because of experimentally inaccessible energy value of the Al K-edge (1.560 keV), EXAFS did not allow to measure the Al-centered local structure. It is noteworthy that the EXAFS measurement also requires a proper transmission thickness. Therefore, both the ribbon sample and the slice cut from the rod were polished manually till its thickness was 30–40 μm. These EXAFS raw data were normalized via a standard data-reduced procedure, employing the Visual Processing in EXAFS Researches (VIPER) [26].

2.3 Molecular Dynamics Simulation upon Reverse Monte-Carlo Fitting

The reverse Monte Carlo (RMC) fitting technique [27] is an iterative method extensively used for building the possible structural models, so that we can probe the detailed structural information in disordered systems that agree quantitatively with the available experimental data, in particular the synchrotron radiation-based XRD, EXAFS, and neutron diffraction data [28]. In this work, the synchrotron radiation-based diffraction and EXAFS data were fitted simultaneously in the RMC frame. The initial cubic boxes of the rod and the ribbon models containing 40,000 random-distributed atoms were built, and the atomic density for both models were set to be 0.056805 Å^{-3}, matching the $Zr_{48}Cu_{45}Al_7$ composition. The minimum interatomic distances of Zr–Zr, Zr–Cu, Zr–Al, Cu–Cu, Cu–Al, and Al–Al pairs are 2.85 Å, 2.50 Å, 2.40 Å, 2.25 Å, 2.25 Å, and 2.35 Å, respectively. Once the simulation data fit well with the experimental ones, the RMC fitting is stopped, and atomistic structural models denoting both rod and ribbon samples are obtained, in which all the atoms are "frozen" with determined three-dimensional positions.

It is known that molecular dynamics (MD) simulation is a powerful tool for studying the microstructures and deformation behaviors in MGs, while this method usually lacks the fitting to experimental data [29–33]. Meanwhile, RMC simulation fitting the synchrotron radiation experimental data can probe fine structural information in MGs, while it lacks the chemical potential that can avoid uncertainties during calculation or simulation [14, 28, 34–36]. In this work, to obtain a reliable structure model, a feasible scheme was adopted to combine the RMC fitting with the MD simulation, is similar to that applied for studying MGs in previous work [37, 38]. Based on the structural model obtained from RMC fitting the synchrotron-radiation XRD and EXAFS data, a further MD simulation was performed to modify this model, so that both computational (e.g., iterative fitting) and physical (e.g., chemical potential) considerations were included [39]. This MD simulation was carried out by employing the program of large-scale atomic/molecular massively parallel simulator (LAMMPS) [40], based on the embedded atom method (EAM) potential developed by Cheng et al. [41] The structural model obtained from RMC fitting was relaxed for 2 ns at 300 K under periodic boundary conditions (PBCs), within an NPT (constant number, constant pressure, and constant temperature) ensemble [42], and the Nose–Hoover thermostat and Parrinello–Rahman technique were adopted to control the temperature and pressure. Finally, their modified and stabilized structural models were obtained. We stress that, although the rod and the ribbon samples have different sizes caused by different cooling rates, their as-constructed structural models have almost the same size, So that any influence of the size effect in these two models during the following deformation simulated by MD method can be excluded.

2.4 Deformation by MD Simulation

The as-constructed model was enlarged by replicating itself along the X-direction for three times, so that we can study the compression process in the enlarged model. In order to solve the problem of the structural instability caused by the reproduction of these cubic models, this enlarged model which contained about 120,000 atoms was relaxed via a further short-time MD simulation for about 200 ps at 300 K within the NPT ensemble under PBCs along X- and Y-directions, while the boundaries of Z-direction were changed into free surfaces. Subsequently, this enlarged model after relaxation was deformed by applying a uniaxial compressive strain at a rate of 1×10^8 s^{-1} along the X-direction at a constant temperature of 300 K, and the same boundaries conditions of Y- and Z-directions were applied during the relaxation process. As a result, the evolution of the enlarged structural model during deformation could be studied.

It is noted that such computational simulation is capable of revealing trends and mechanisms, although the simulated properties do not necessarily reproduce the values in experiments, due to the small model size, the high strain rate, and other simulation constraints limitations in MD [8, 43]. They only serve for a qualitative analysis of the possible impact of the cooling rates on the mechanical strength of a MG, and link structure details with properties.

3 Results and Discussion

3.1 Simulation upon Synchrotron Radiation Data

Figure 1 shows the S(Q) curves and the total distribution functions, G(r)s. Both of them were obtained from the synchrotron radiation XRD experiment. Compared with the routine lab experiments, the synchrotron radiation-based XRD measurements could be more reliable to detect the fine structure features in amorphous materials. The absence of any sharp peak behind the first strong peak in the S(Q) curves and the smooth oscillations in the G(r) data adequately

indicate the full amorphous nature in both samples [44]. Although the overall shape in both of the S(Q) and the G(r) curves are similar in these two models, it is found that there are fine differences in their first-, second- and third-shell distributions, in terms of the peak intensity, position, and width, implying that there are some fines structural changes caused by the different cooling rates.

Based on the as-constructed models obtained via MD simulation modifying the RMC fitting result, theoretical S(Q) curves and even Zr and Cu K-edge EXAFS data could be calculated. Figure 2 shows the calculated S(Q) curves, the Cu and Zr K-edge EXAFS spectra, as well as their corresponding experimental data. The good matching between all the experiment-simulation pairs confirms the reliability of these two as-constructed models.

3.2 Stress and Strain

The simulated uniaxial compressive stress–strain curves of both ribbon and rod models with the composition of $Zr_{48}Cu_{45}Al_7$, are plotted in Fig. 3. It is found that when the strain is lower than 4%, there is a linear relationship between strain and stress in both rod and ribbon models, indicating an elastic deformation stage, within which there is no significant difference of the Young's modulus between the ribbon and the rod models, suggesting that the cooling rate does not affect the elastic stage. This is consistent with the previous work [14]. When the strain is more than 4%, the rise of the stress values becomes slow, indicating an inelastic deformation. The stress reaches a maximum value at a strain about 7%, denoting the yield strength in both rod and ribbon models. It is interesting that the rod model has a large yield strength about 2.67 GPa, while the ribbon one has a small yield strength about 2.50 GPa, implying a strengthening effect caused by relatively low cooling rate, is in accord with previous work [8, 45].

When the strain goes on increasing, the stress decreases instead. Nevertheless, when the strain reaches a critical value about 16%, the stress is no longer decreased and keeps a constant at the high strain range. It is notable that there are

Fig. 1 The synchrotron radiation-based XRD data of both $Zr_{48}Cu_{45}Al_7$ samples, including: **a** the normalized structure factor, S(Q), and **b** the total pair distribution function, G(r)
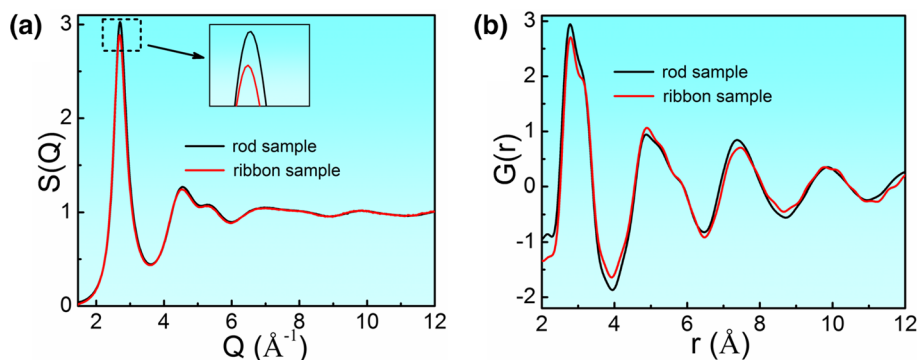
Fig. 2 Structural information, including **a** the simulated three-dimensional atomic configuration of the ribbon model (the corresponding atomic configuration of the rod sample is not shown here); **b** the S(Q), **c** Cu K-edge and **d** Zr K-edge EXAFS spectra. The solid and the dashed lines denote experimental and simulation data, respectively. Zr, Cu, and Al atoms are shown in yellow, blue, and red colors, respectively. κ and $\chi(\kappa)$ represent the photoelectron wave vector and the k-space EXAFS signals, respectively. This simulation was performed by MD simulation to modify the RMC fitting data
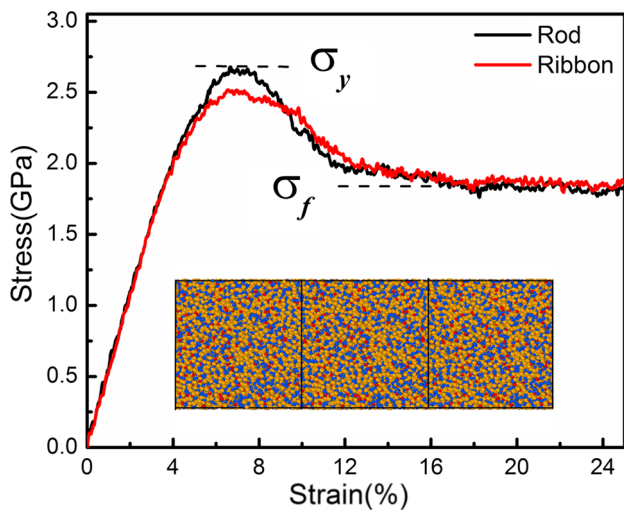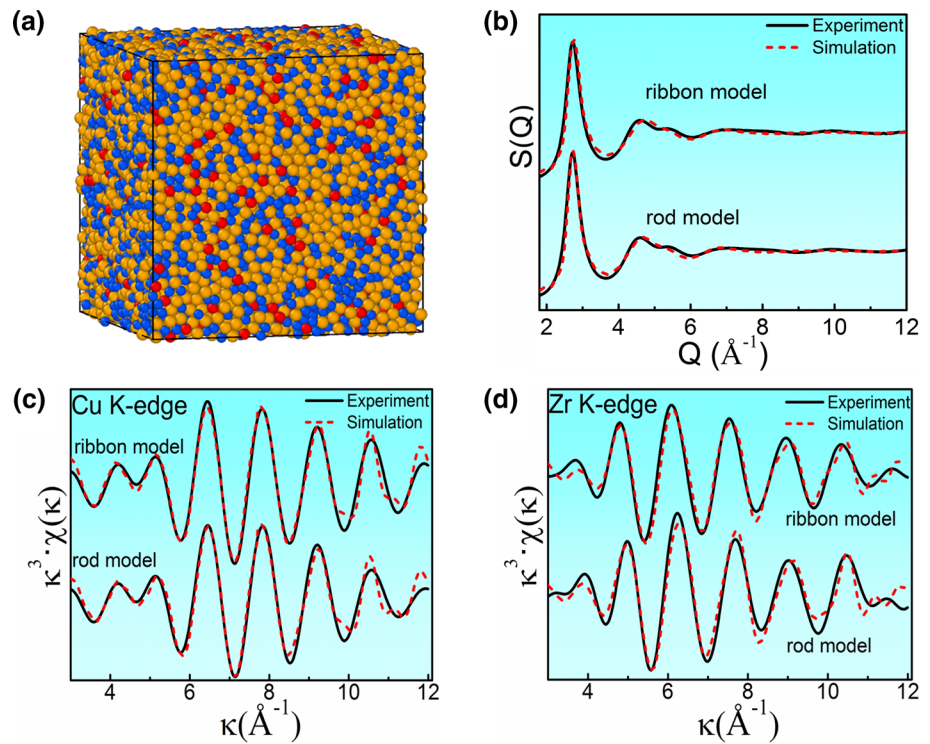
Fig. 3 The MD simulated uniaxial stress–strain curves of these two $Zr_{48}Cu_{45}Al_7$ structural models under a compressive deformation. The insert is the enlarged model

two characteristic stresses in these two curves: the overshoot stress of for yielding, σ_y, and the quasi-steady flow stress, σ_f [32]. It was suggested that σ_y reflects the intrinsic resistance to flow initiation, and σ_f denotes the shear resistance of the rejuvenated quasi-steady flow state or the shear traction provided by the rejuvenated glass structure [8]. The stress gap between σ_f and σ_y ($\Delta\sigma = \sigma_y - \sigma_f$) indicates the degree of softening during the deformation, and its magnitude reflects

a tendency to strain localization in the flow region. These parameters are related to the plasticity of MGs: the higher resistance of plastic flow (higher σ_f and σ_y) and more tendency to strain localization (larger $\Delta\sigma$), the less the plasticity is.

It is worth noting that, although the σ_y value (2.67 GPa) of the rod model is higher than that (2.50 GPa) of the ribbon model, both of these two models have the same σ_f value, 1.85 GPa. In other words, the stress gap between σ_f and σ_y of the rod model has a value of 0.82 GPa, is apparently larger than the counterpart (0.65 GPa) of the ribbon model. This is an evidence that low cooling rate leads to the deterioration of plasticity, because the plasticity decreases with the increase of such stress gap. In addition, the stress of the rod model drops more rapidly during the softening process, and is close to the quasi-steady flow stress at a smaller strain value than the ribbon one, implying that a MG prepared with a relatively low cooling rate is more likely to soften itself.

3.3 The Cluster-Level Structural Information

3.3.1 Coordination Number

It is known that the deformation is accompanied by the short-range structure evolutions under stress applied [8, 32, 46–48]. Therefore, the short-range structural evolution should be tracked at the cluster scale. A cluster with one center atom and some shell atoms is regarded as a structural unit that can indicate the local structure feature of MGs. By

using the Voronoi tessellation, we can deduce all the Voronoi clusters (VCs) in a MG structural model [28, 49]. The cut-off value for extracting a VC was about 3.90 Å, according to the maximum radial value of the first-shell distribution of G(r), as shown in Fig. 1. It was suggested that atoms densely packed inside a cluster can lead to relatively large number of shell atoms, i.e., the coordination number (CN) [38]. The relationship between the CN of VCs and the strain is shown in Fig. 4. It is found that, with the increase of strain, the CN values decreases in both models, implying that the compressive deformation leads to densely atomic packing in MGs. Nevertheless, when the strain reaches about 14%, i.e., the beginning of the quasi-steady flow stage, CN value no longer decreases with the strain, suggesting that atoms cannot be more densely packed in clusters. In addition, it is worth noting that the CN values of the rod model are always
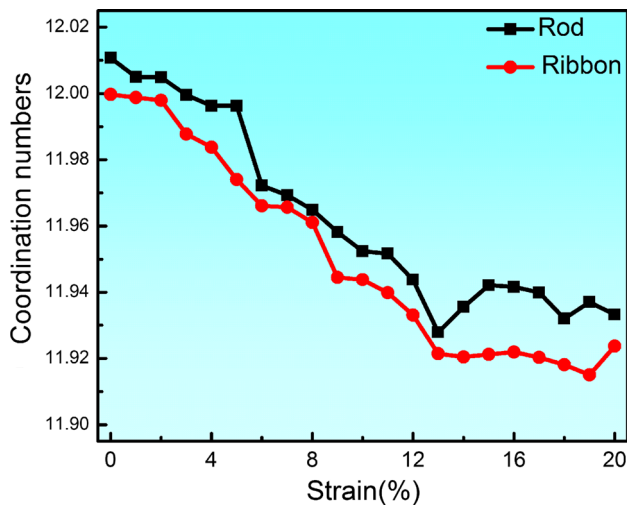
larger than their counterparts of the ribbon sample during the deformation. This indicates that higher cooling rate leads to denser atomic packing, and this tendency is unlikely to change during the deformation process.

3.3.2 Concentration of Clusters

It was suggested that <0,0,12,0> VC which is the so-called full icosahedron that possesses 12 fivefold symmetries and some other icosahedral-like clusters such as <0,1,10,2>, are the indicators of high shear resistance, high packing density, and low potential energy [50]. They are very sensitive to the cooling rate and the stress. Figure 5 shows the distribution of <0,0,12,0> and <0,1,10,2> VCs extracted from the ribbon and the rod models during the compressive deformation. It is found that, with the increase of strain, the fraction of <0,0,12,0> drops dramatically, and does not apparently change when the strain until it reaches about 14%, i.e., the beginning of quasi-steady flow state. Regarding the fraction of <0,1,10,2> VC, although it does not change as dramatically as that of <0,0,12,0>, it also decreases slightly and no longer changes when the strain reaches about 14%. This implies that these two dense-packing clusters are apt to transform into relatively loose-packing clusters when a compressive stress is loaded. However, such cluster-level transformation stops at the beginning of quasi-steady flow state.

Furthermore, it is worth noting that, although the relationship between these two VCs and the strain is almost the same in both ribbon and rod samples, the fractions of <0,0,12,0> and <0,1,10,2> VCs in the rod model are always larger than their counterparts of the ribbon model at each strain point, suggesting that lower cooling rate does lead to more dense-packing clusters, no matter in the as-prepared or the deformed MG models. As shown in Fig. 3, a lower cooling rate leads to a higher yield strength and makes it more


Fig. 4 Relationship between the coordination numbers and the strain in these two models
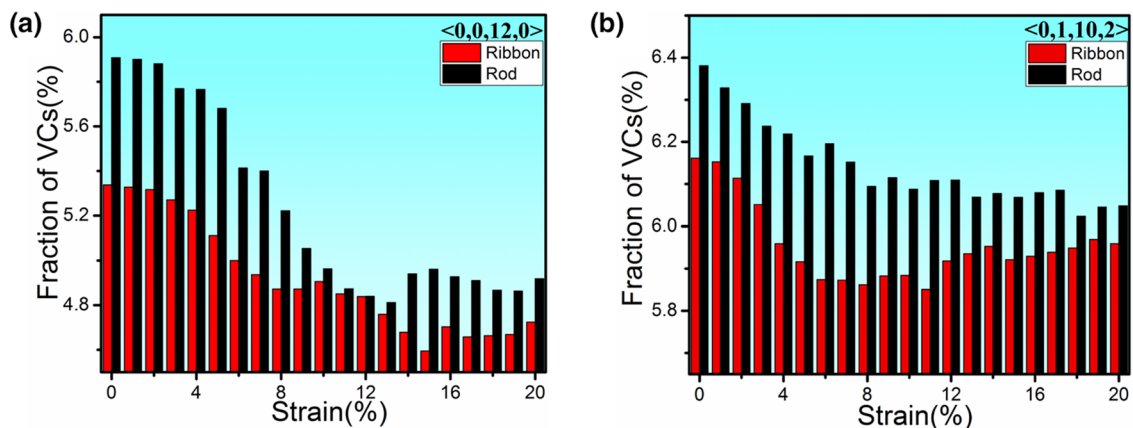
Fig. 5 Distribution of some major Voronoi clusters (VCs) such as **a** <0,0,12,0> and **b** <0,1,10,2> extracted from the ribbon and the rod models during the compressive deformation

difficult to trigger the plastic flow. Therefore, <0,0,12,0> and <0,1,10,2> VCs should be regarded as important structure parameters to resist the shear deformation, and the decrease of which leads to the post-yield strain-softening, and such cluster-level contribution is significantly influenced by the cooling rate.

3.3.3 Regularity of Clusters

Although clusters can be extracted from MG structural models by using some indexing methods such as Voronoi tessellation, it is questionable that the cluster concentration can be used for evaluating the contribution of local structures to the glass formation and the deformation behaviors in MGs [8, 32, 46]. This is because such index is not yet perfectly accurate, but determined by the symmetries of the shell atoms in each cluster, so that the cluster regularity affected by the bond lengths, the bond angles, or the chemical fluctuation of shell atoms, is not considered. Clusters can adjust their geometric regularities without changing their Voronoi indexation, because this is not required to overcome a relatively big barrier [51, 52]. The adjustment of geometric regularities in clusters apparently affects the cluster volume and the atomic packing involved. Therefore, the regularity of VCs may be an important structural feature reflecting the effect of the cooling rate on the microstructural evolution in MGs during the deformation process. To verify this scenario, a regularity parameter of clusters [28, 53], T, is adopted, and its correlation with the strain is established and shown in Fig. 6.

For a regular tetrahedron where all edges are the same in length, the value of T should be zero. It is found that there is a tight relationship between the regularity parameter and
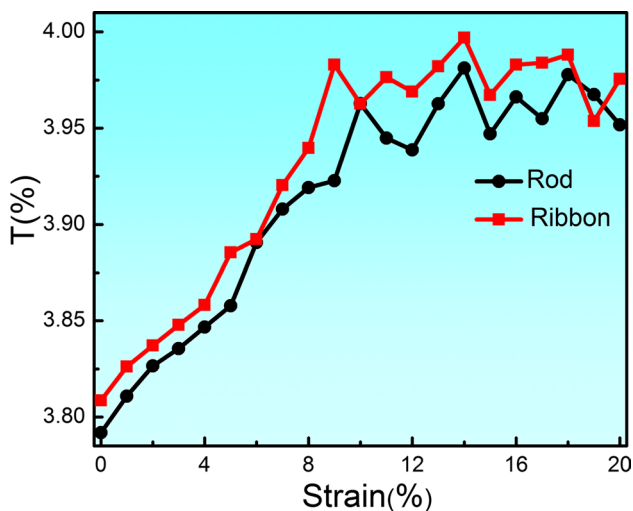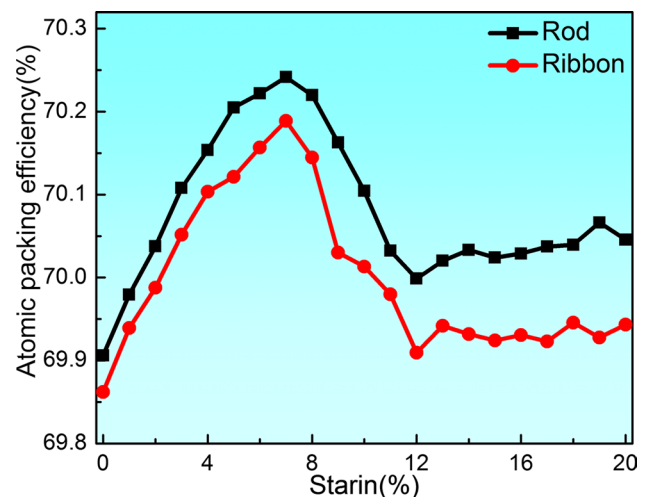
the strain. The regularity parameter increases dramatically and monotonously when the strain is less than 10%, suggesting that clusters are easy to become more irregular under the compressive stress. When the strain goes on increasing, the regularity parameter does not apparently increase, but exhibits a slight fluctuation. This indicates that clusters are likely to fix themselves geometrically in the quasi-steady flow state. In addition, it is found that the cluster regularity-strain curves of both models are very similar with each other, while the regularity parameter of the ribbon model has a larger value than its counterpart of the rod sample at each strain point. This hints that a high cooling rate contributes to a low degree of regularity, and yet the evolution of cluster regularity during the compressive deformation is apparently independent of the cooling rate.

3.4 Atomic Packing Efficiency

Although the evolution of atomic packing with the strain could be evaluated by the CNs, the VC concentrations, as well as the degree of regularity, it is still difficult to directly indicate the global atomic packing and its contribution to the deformation. The atomic packing efficiency (APE) which is defined as the volume fraction of atoms, has been recognized as a key structural parameter linked up with both glass formation and deformation in MGs [28]. Therefore, studying the change of APE values during the compression process also is required. A method to quantitatively calculate the APE has been developed in our previous work [28], and was used in this work. It is found that the relationship between the APE and the strain (as shown in Fig. 7) are very similar to the strain–stress curves that are shown in Fig. 3. At first, the APE increases monotonously with the increase of strain for both models. At the elastic stage where the stain is below 4%, the APE increases linearly with

Fig. 6 Relationship between the cluster regularity parameter and the strain. The variance of the edge lengths, T, of all the tetrahedra forming clusters is a cluster regularity parameter. Note a smaller T value indicates a higher cluster regularity

Fig. 7 Relationship between the atomic packing efficiency and the strain in both ribbon and rod models

the strain. When the strain exceeds 4%, the increase of APE slows down till the strain reaches a maximum value of 7% corresponding to the yield stress, where atoms are most densely packed in both models. When the strain goes on increasing, the resistance of the initiation of plastic flow is weakened, leading to the transition of dense-to-loose atomic packing. Therefore, APE decreases instead until it reaches a plateau, which corresponds to the post-yield strain-softening and the quasi-steady flow stages, respectively. In addition, it is noted the APE of the rod model is higher than that of the ribbon model during the compression process, implying that smaller cooling rate leads to a denser atomic packing in their local structures. This tendency is consistent with evolutions of both the cluster concentration and the cluster regularity.

The APE is a global parameter that can reflect the intrinsic structural features in MGs, no matter how atoms arrange themselves topologically or chemically. Therefore, the relationship between the APE and the strain established in this work directly indicates how microstructure controls or affects the deformation when a compressive stress is loaded, and is tightly related to the elastic, the yielding, the softening, and the quasi-steady flow stages. In addition, the lower cooling rate plays an important role in increasing the APE values, accompanying by the strengthen effect and the higher resistance of plastic flow.

3.5 Free Volume

The free volume concept proposed by Cohen and Turnbull [54–56], is widely used to explain many significant issues of structure and properties in MGs, such as short-range structure, medium-range structure, flow deformation, glass formation, mechanical properties, and so on. The free volume concept is related to APE, because free volumes are involved in the void spaces that are not occupied by atoms. However, how to quantitatively characterize free volumes experimentally is still a challenge. Recently, according to definition of free volume, a lot of algorithms have been applied for calculating free volumes quantitatively and accurately at the atomic level [57–60]. In our previous work [48], a computational method to estimate free volumes quantitatively in amorphous alloys has been developed, and was adopted in this work.

Unlike crystal alloys with well-defined structure units (unit cells) and well-defined defects (point defects and dislocations) that are sensitive to deformation, it has been proposed that some other "defects" such as free volumes affect the deformation of MGs. Figure 8 displays the relationship between the strain and the fraction of free volumes, which is calculated from this expression,

$$FFV = \frac{\sum FV}{V} \tag{2}$$
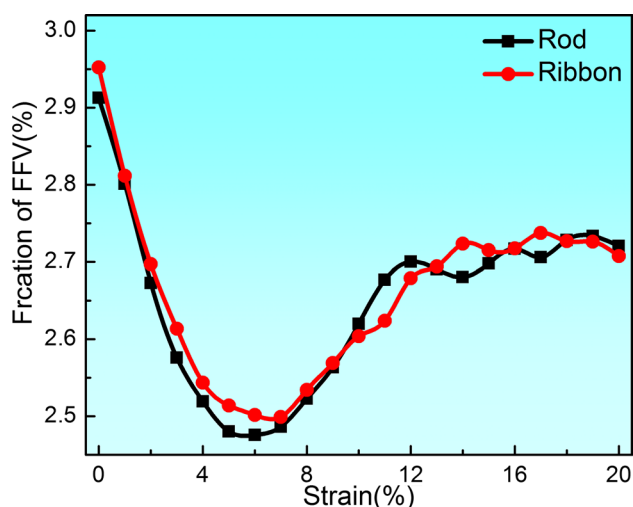
Fig. 8 Evolution of the fraction of free volumes (FFV) during the compressive deformation

FFV, FV, and V denote the fraction of the total free volume in the volume of this model, each free volume, and the volume of this model itself, respectively.

It is found that, at the elastic stage where the stain is below 4%, the FFV value in both models decreases monotonically with the increase of strain. When the stain exceeds 4%, the decrease of FFV slows down until the strain reaches a minimum value of 7% which corresponds to the yield strength point. During this process, the FFV value of the rod model is always smaller than those of the ribbon sample.

Especially, the FFV at the strain of 7% in the rod sample is about 2.48%, smaller than the counterpart (2.50%) of the ribbon model. We have revealed that the rod sample has a larger yield strength at the strain of 7%, thus, it indicates that the smaller FFV relates tightly to the larger yield strength. Furthermore, when increasing the strain, the FFV value in both models increases instead, and get to a plateau about 2.7% which has some slight oscillations. This saturation of free volumes at the large strain region just corresponds to the quasi-steady flow state, suggesting that free volumes cannot change any more after the softening. It is interesting that the rod model has a larger gap of FFV from the strain of 7% to at least 12%, is quite consistent with the strain range of the softening process, as shown in Fig. 3. This implies that the change of free volumes relates tightly to the softening process, and the large change of free volumes leads to the large stress gap during the softening, and the plasticity is reduced accordingly. In addition, during this period, the increasing rate of FFV value in the ribbon model is smaller than that of the rod sample, and the FFV reaches a plateau at the strain of 14%, which is larger than that (12%) of the latter. It has been revealed that the stress reaches the quasi-steady flow state at a smaller strain value. Therefore, it implies that the

saturation of free volumes during the compressive deformation can well indicate the beginning of the quasi-steady flow state.

Since it is revealed that the change of free volumes is related to the deformation behaviors in particular the stress–strain relationship, we wonder how free volumes change during the deformation. We suppose that the evolution of free volumes during deformation is affected by several factors. (1) Free volumes are apt to be annihilated by the uniaxial compressive stress; (2) many dense-packed clusters have been collapsed under stress, resulting in new free volumes instead [32]. When a MG is under a compressive stress, the annihilating rate of free volumes is probably larger than the creation rate, leading to the monotonical decrease of FFV value. But this decrease gets slower until the strain increases to 7%, i.e., the yield stress point. When the strain is larger than 7%, the annihilation of free volumes will not catch up with the creation rate, so that the FFV begins to increase instead. When the strain goes on increasing, a balance between the annihilation rate and the creation rate of free volumes will be achieved, free volumes get saturated and the FFV value does not change any more.

Furthermore, deformation events and the free volume parameter are related to the shear transformation zones (STZs), which is a small cluster of randomly close-packed atoms that spontaneously and cooperatively reorganize under the action of an applied shear stress [61–64]. It was proposed that deformation occurs preferentially in the STZs, which are characterized by a lower density of atomic packing [32, 63]. These relatively loose-packing regions provide atoms more free volumes [33], leading to the rich of free volumes in some localized regions in MGs.

Based on the above analysis, the cooling rate effect on the deformation behaviors in MGs can be explained. It is observed that the FFV in the as-constructed ribbon model is higher than that of the rod one, implying that the higher cooling rate contributes to more free volumes. During the rapid quench, the annihilation rate of free volumes is too slow to maintain an equilibrium state, and the excess free volumes will be frozen in MGs, resulting in a larger amount of free volumes that is preserved in the glassy solid. Because of the deficiency of free volumes in the as-constructed rod model that will slow down the creation of STZs during the deformation, a higher stress is required to activate new STZs [64]. The lower density of STZs enhances the yield strength and leads to reduced plasticity in MGs [33]. In previous work [65], it was reveals that the higher stress would induce a fast creation of free volumes, leading to a strain softening. In short, it is concluded that the different FFV values in as-constructed structural models obtained by quenching the melt at different cooling rates do affect the formation and evolution of STZs, as well as the yield strength and the plasticity.

In addition, we stress that: (1) the size effect was completely excluded in this work, because the experimental measurement and the simulation work were performed by using the same size for both rod and ribbon samples, although they had different original casting sizes or dimensions; (2) since positions of all atoms in each model in the as-prepared state or during the deformation could be precisely determined, and the calculations of coordination numbers, VC distributions, VC regularity, atomic packing efficiency, or free volumes, were performed via the same procedure or standard in both models. Such calculation work is capable of revealing trends and mechanisms of the effect of cooling rate on the microstructures or the deformation in MGs.

4 Conclusions

In summary, the microstructures linked up with the deformation behaviors in two $Zr_{48}Cu_{45}Al_7$ MGs prepared at different cooling rates were studied, by using the synchrotron radiation-based experiments coupled with a series of simulations. Although there is no significant difference in Young's modulus between these two models, the lower cooling rate leads to the higher yield strength in a MG model, and is more likely to soften this model, resulting in the lower plasticity. It is found that some structural parameters such as coordination numbers, atomic packing efficiencies, cluster concentrations and regularities, are apparently different between these two models in the as-constructed state, while their evolutions during the compressive deformation are very similar. In addition, the evolutions of the fraction of free volumes in these two models are different during the compressive deformation, affecting the initiation and the evolution of STZs, as well as the yield strength and the plasticity. Especially, the rod sample prepared at a lower cooling rate corresponds to higher yield strength and relatively poor plasticity. This work will shed light on the essential mechanisms of deformation behaviors and microscopic deformation in MGs prepared at different cooling rates.

Compliance with Ethical Standards

Conflict of interest The authors declare that they have no conflict of interest.

References

1. P. Duwez, R.H. Willens, W. Klement, J. Appl. Phys. **31**, 1136–1137 (1960)
2. L. Reichel, L. Schultz, D. Pohl, S. Oswald, S. Fahler, M. Werwinski, A. Edstrom, E.K. Delczeg-Czirjak, J. Rusz, J. Phys. Condens. Matter **27**, 476002 (2015)
3. H.Y. Jung, S.J. Choi, K.G. Prashanth, M. Stoica, S. Scudino, S. Yi, U. Kühn, D.H. Kim, K.B. Kim, J. Eckert, Mater. Des. **86**, 703–708 (2015)
4. C. Zhang, R.Q. Guo, Y. Yang, Y. Wu, L. Liu, Electrochim. Acta **56**, 6380–6388 (2011)
5. C. Schuh, T. Hufnagel, U. Ramamurty, Acta Mater. **55**, 4067–4109 (2007)
6. S.V. Ketov, Y.H. Sun, S. Nachum, Z. Lu, A. Checchi, A.R. Beraldin, H.Y. Bai, W.H. Wang, D.V. Louzguine-Luzgin, M.A. Carpenter, A.L. Greer, Nature **524**, 200–203 (2015)
7. W.H. Wang, C. Dong, C.H. Shek, Mater. Sci. Eng. R **44**, 45–89 (2004)
8. Y.Q. Cheng, A.J. Cao, H.W. Sheng, E. Ma, Acta Mater. **56**, 5263–5275 (2008)
9. J. Wang, P.D. Hodgson, J. Zhang, W. Yan, C. Yang, J. Mater. Process. Technol. **209**, 4601–4606 (2009)
10. H. Li, G.H. Wang, J.J. Zhao, X.F. Bian, J. Chem. Phys. **116**, 10809–10815 (2002)
11. L. Yang, G.Q. Guo, L.Y. Chen, B. LaQua, J.Z. Jiang, Intermetallics **44**, 94–100 (2014)
12. Y.J. Huang, J. Shen, J.F. Sun, Appl. Phys. Lett. **90**, 081919 (2007)
13. Y. Liu, H. Bei, C.T. Liu, E.P. George, Appl. Phys. Lett. **90**, 071909 (2007)
14. Z.Y. Liu, Y. Yang, S. Guo, X.J. Liu, J. Lu, Y.H. Liu, C.T. Liu, J. Alloys Compd. **509**, 3269–3273 (2011)
15. C. Li, S. Kou, Y. Zhao, G. Liu, Y. Ding, Prog. Nat. Sci. **22**, 21–25 (2012)
16. Y. Hu, H.H. Yan, Z.J. Yan, X.G. Wang, AIP Adv. **8**, 105002 (2018)
17. Y. Yokoyama, K. Yamano, K. Fukaura, H. Sunada, A. Inoue, Scr. Mater. **44**, 1529–1533 (2001)
18. R.D. Conner, W.L. Johnson, N.E. Paton, W.D. Nix, J. Appl. Phys. **94**, 904–911 (2003)
19. W.H. Jiang, F.X. Liu, Y.D. Wang, H.F. Zhang, H. Choo, P.K. Liaw, Mat. Sci. Eng. A **430**, 350–354 (2006)
20. W.B. Liao, Y.Y. Zhao, J.P. He, Y. Zhang, J. Alloys Compd. **555**, 357–361 (2013)
21. X.H. Lin, W.L. Johnson, J. Appl. Phys. **78**, 6514–6519 (1995)
22. D. Wang, H. Tan, Y. Li, Acta Mater. **53**, 2969–2979 (2005)
23. N.H. Pryds, X. Huang, Metall. Mater. Trans. A **31**, 3155–3166 (2000)
24. A.P. Hammersley, S.O. Svensson, M. Hanfland, A.N. Fitch, D. Hausermann, High Pressure Res. **14**, 235–248 (1996)
25. T.E. Faber, J.M. Ziman, Philos. Mag. **11**, 153–173 (1965)
26. M. Felderhoff, K. Klementiev, W. Grunert, B. Spliethoff, B. Tesche, J.M. Bellosta von Colbe, B. Bogdanovic, M. Hartel, A. Pommerin, F. Schuth, C. Weidenthaler, Phys. Chem. Chem. Phys. **6**, 4369–4374 (2004)
27. R.L. McGreevy, J. Phys. Condens. Matter **13**, R877–R913 (2001)
28. L. Yang, G.Q. Guo, L.Y. Chen, C.L. Huang, T. Ge, D. Chen, P.K. Liaw, K. Saksl, Y. Ren, Q.S. Zeng, B. LaQua, F.G. Chen, J.Z. Jiang, Phys. Rev. Lett. **109**, 105502 (2012)
29. S. Ogata, F. Shimizu, J. Li, M. Wakeda, Y. Shibutani, Intermetallics **14**, 1033–1037 (2006)
30. G. Duan, D. Xu, Q. Zhang, G. Zhang, T. Cagin, W.L. Johnson, W.A. Goddard, Phys. Rev. B **74**, 019901 (2006)
31. Y.L. Sun, J. Shen, A.A. Valladares, J. Appl. Phys. **106**, 073520 (2009)
32. K.W. Park, E. Fleury, H.K. Seok, Y.C. Kim, Intermetallics **19**, 1168–1173 (2011)
33. S.D. Feng, K.C. Chan, L. Zhao, S.P. Pan, L. Qi, L.M. Wang, R.P. Liu, Mater. Des. **158**, 248–255 (2018)
34. N. Mattern, P. Jóvári, I. Kaban, S. Gruner, A. Elsner, V. Kokotin, H. Franz, B. Beuneu, J. Eckert, J. Alloys Compd. **485**, 163–169 (2009)
35. P. Jóvári, I. Kaban, B. Escher, K.K. Song, J. Eckert, B. Beuneu, M.A. Webb, N. Chen, J. Non-Cryst. Solids **459**, 99–102 (2017)
36. K. Itoh, J. Saida, T. Otomo, J. Alloys Compd. **732**, 585–592 (2018)
37. P.W. Wang, H.Y. Li, L. Yang, Metals **7**, 444 (2017)
38. B.F. Lu, L.T. Kong, K.J. Laws, W.Q. Xu, Z. Jiang, Y.Y. Huang, M. Ferry, J.F. Li, Y.H. Zhou, Mater. Charact. **141**, 41–48 (2018)
39. L. Yang, H.Y. Li, P.W. Wang, S.Y. Wu, G.Q. Guo, B. Liao, Q.L. Guo, X.Q. Fan, P. Huang, H.B. Lou, F.M. Guo, Q.S. Zeng, T. Sun, Y. Ren, L.Y. Chen, Sci. Rep. **7**, 16739 (2017)
40. S. Plimpton, J. Comput. Phys. **117**, 1–19 (1995)
41. Y.Q. Cheng, E. Ma, H.W. Sheng, Phys. Rev. Lett. **102**, 245501 (2009)
42. W.G. Hoover, Phys. Rev. A **31**, 1695–1697 (1985)
43. T. Frolov, K.A. Darling, L.J. Kecskes, Y. Mishin, Acta Mater. **60**, 2158–2168 (2012)
44. Q. Zeng, H. Sheng, Y. Ding, L. Wang, W. Yang, J.Z. Jiang, W.L. Mao, H.-K. Mao, Science **332**, 1404–1406 (2011)
45. Y. Xiao, Y. Wu, Z. Liu, H. Wu, Z. Lü, Sci. China Phys. Mech. **53**, 394–398 (2010)
46. M. Wakeda, Y. Shibutani, S. Ogata, J. Park, Intermetallics **15**, 139–144 (2007)
47. H.L. Peng, M.Z. Li, W.H. Wang, Phys. Rev. Lett. **106**, 135503 (2011)
48. W. Da, P.W. Wang, Y.F. Wang, M.F. Li, L. Yang, Materials **12**, 98 (2019)
49. J.L. Finney, D. Bernal John, Proc. R. Soc. London Ser. A **319**, 479–493 (1970)
50. A.P. Tsai, Sci. Technol. Adv. Mater. **9**, 013008 (2008)
51. X.K. Xi, L.L. Li, B. Zhang, W.H. Wang, Y. Wu, Phys. Rev. Lett. **99**, 095501 (2007)
52. S.Y. Wang, M.J. Kramer, M. Xu, S. Wu, S.G. Hao, D.J. Sordelet, K.M. Ho, C.Z. Wang, Phys. Rev. B **79**, 144205 (2009)
53. N.N. Medvedev, Y.I. Naberukhin, J. Non-Cryst. Solids **94**, 402–406 (1987)
54. M.H. Cohen, D. Turnbull, J. Chem. Phys. **31**, 1164–1169 (1959)
55. D. Turnbull, M.H. Cohen, J. Chem. Phys. **34**, 120–125 (1961)
56. D. Turnbull, M.H. Cohen, J. Chem. Phys. **52**, 3038–3041 (1970)
57. J. Sietsma, B.J. Thijsse, Phys. Rev. B **52**, 3248–3255 (1995)
58. F. Li, X.J. Liu, H.Y. Hou, G. Chen, G.L. Chen, M. Li, Intermetallics **17**, 98–103 (2009)
59. Y. Zhang, H. Hahn, J. Non-Cryst. Solids **357**, 1420–1425 (2011)
60. X.X. Yue, C.T. Liu, S.Y. Pan, A. Inoue, P.K. Liaw, C. Fan, Physica B **547**, 48–54 (2018)
61. A.S. Argon, Acta Metall. **27**, 47–58 (1979)
62. A.S. Argon, J. Phys. Chem. Solids **43**, 945–961 (1982)
63. Y. Shi, M.B. Katz, H. Li, M.L. Falk, Phys. Rev. Lett. **98**, 185505 (2007)
64. S.D. Feng, W. Jiao, S.P. Pan, L. Qi, W. Gao, L.M. Wang, G. Li, M.Z. Ma, R.P. Liu, J. Non-Cryst. Solids **430**, 94–98 (2015)
65. M.Q. Jiang, G. Wilde, L.H. Dai, Mech. Mater. **81**, 72–83 (2015)